Monthly Notices of the ROYAL ASTRONOMICAL SOCIETY

MNRAS **523,** 5198–5206 (2023) https://doi.org/10.1093/mnras/stad1773
Advance Access publication 2023 June 14

3D evolution of neutron star magnetic fields from a realistic core-collapse turbulent topology

Clara Dehman [1,2]★ Daniele Viganò [1,2,3] Stefano Ascenzi,[1,2] Jose A. Pons[4] and Nanda Rea [1,2]

[1]*Institute of Space Sciences (ICE-CSIC), Campus UAB, Carrer de Can Magrans s/n, E-08193 Barcelona, Spain*
[2]*Institut d'Estudis Espacials de Catalunya (IEEC), Carrer Gran Capitá 2–4, E-08034 Barcelona, Spain*
[3]*Institute of Applied Computing & Community Code (IAC3), University of the Balearic Islands, E-07122 Palma, Spain*
[4]*Departament de Física Aplicada, Universitat d'Alacant, Ap. Correus 99, E-03080 Alacant, Spain*

Accepted 2023 June 9. Received 2023 June 9; in original form 2023 May 10

ABSTRACT

We perform the first 3D fully coupled magneto-thermal simulations of neutron stars (including the most realistic background structure and microphysical ingredients so far) applied to a very complex initial magnetic field topology in the crust, similar to what was recently obtained by proto-neutron stars dynamo simulations. In such configurations, most of the energy is stored in the toroidal field, while the dipolar component is a few per cent of the mean magnetic field. This initial feature is maintained during the long-term evolution ($\sim 10^6$ yr), since the Hall term favours a direct cascade (compensating for Ohmic dissipation) rather than a strong inverse cascade, for such an initial field topology. The surface dipolar component, responsible for the dominant electromagnetic spin-down torque, does not show any increase in time, when starting from this complex initial topology. This is in contrast to the timing properties of young pulsars and magnetars which point to higher values of the surface dipolar fields. A possibility is that the deep-seated magnetic field (currents in the core) is able to self-organize in large scales (during the collapse or in the early life of a neutron star). Alternatively, the dipolar field might be lower than is usually thought, with magnetosphere substantially contributing to the observed high spin-down, via e.g. strong winds or strong coronal magnetic loops, which can also provide a natural explanation to the tiny surface hotspots inferred from X-ray data.

Key words: stars: evolution – stars: interiors – stars: magnetars – stars: magnetic field – stars: neutron.

1 INTRODUCTION

In the last years, increasing efforts have been dedicated to magnetohydrodynamical (MHD) simulations of core-collapse supernovae (CCSN) (e.g. Mösta et al. 2014, 2015; Obergaulinger, Janka & Aloy 2014; Bugli et al. 2020; Aloy & Obergaulinger 2021; Obergaulinger & Aloy 2022; Powell et al. 2023). Besides the intrinsic importance in understanding the underlying explosion mechanisms and the fundamental physics of hot dense matter (Janka 2012; Obergaulinger & Aloy 2020), CCSN simulations are important to define the characteristics of its compact remnant, a hot proto-neutron star (PNS, e.g. Pons et al. 1999; Barrère et al. 2022). The highly dynamical process consists of three main stages: (i) For about 1 s after the core bounce, the system consists of a relatively cool central region surrounded by a hot mantle, collapsing and radiating off neutrinos quickly while still also accreting material. (ii) Over the next ∼20 s, a slowly developing state of the PNS can be identified; the system first deleptonizes and heats up the interior parts of the forming star, and later it cools down further through neutrino diffusion. The PNS is born extremely hot and liquid ($T \approx 10^{10}$ K), with a relatively large radius of ∼100 km. (iii) After several minutes, it becomes transparent to neutrinos and shrinks to its final radius $R \sim$ 10–14 km (Burrows & Lattimer 1986; Keil & Janka 1995; Pons et al. 1999). Neutrino transparency marks the birth of an NS, which starts its long-term cooling, dominated first by neutrinos and later ($t \gtrsim 10^5$ yr) by photon emission from the surface.

The NS magnetic field configuration at birth is largely unknown, and explaining how to generate strong dipolar fields able to explain the timing properties of magnetars is still an open question (see e.g. Igoshev, Popov & Hollerbach 2021b for a review). Different scenarios were discussed in the literature to explain the origin of the magnetic field in magnetars. Magnetic flux conservation can lead to the strongest magnetic fields in the case of highly magnetized progenitors that could be formed in stellar mergers (Ferrario & Wickramasinghe 2006; Schneider et al. 2019; Makarenko, Igoshev & Kholtygin 2021), although it may not explain the formation of millisecond magnetars since highly magnetized progenitors are slow rotators (Shultz et al. 2018). In order to have a fast rotation and a strong magnetic field, a possible scenario is the magnetic field amplification by a turbulent dynamo in the PNS (Raynaud et al. 2020). Different approaches of MHD local or global simulations have been recently put forward to quantify the magnetic field amplification.

On one hand, box simulations with simplified background fields showed the development of the magneto-rotational instability (Balbus & Hawley 1991; Akiyama et al. 2003; Obergaulinger et al. 2014; Rembiasz et al. 2017; Aloy & Obergaulinger 2021). On the other hand, global simulations have explored the PNS dynamo mechanisms (Raynaud et al. 2020; Reboul-Salze et al. 2021; Masada, Takiwaki &

★ E-mail: c.dehman@csic.es

Kotake 2022), including the effects of differential and rigid rotation and convection. As usual in dynamo simulations, the system reaches an equilibrium configuration in which, although the fields are not static at all, the distribution of energy over the scales (or multipoles) is statistically at (quasi)-equilibrium due to the balance between the overall forces in the magnetized fluid. In particular, the magnetic energy of the PNS spreads over a wide range of spatial scales, with non-axisymmetric and toroidal components dominating over the poloidal large-scale dipole. The total energy is compatible with magnetar-like magnetic fields, but it is dominated by the small scales.

In this sense, the approach and results of these studies represent a major advance that improves the highly simplified pictures of static idealized equilibria known as twisted torus, often used as initial field configurations. As a matter of fact, such purely large-scale and axisymmetric configurations have a completely different spatial distribution of the magnetic energy, compared to the dynamo configurations, but they have been often used as starting point for the long-term evolution in NSs. See Becerra et al. (2022) for recent attempts with a random initially complex magnetic field configurations.

Here, we present the first 3D coupled magneto-thermal simulation having at the same time a realistic background structure and microphysics, and an initial magnetic field topology similar (in terms of spectral distribution) to Reboul-Salze et al. (2021). The simulation is performed using *MATINS* (Dehman et al. 2023a & Ascenzi et al. in preparation). The latter works used the most recent temperature-dependent microphysical calculations, a star structure coming from a realistic equation of state (EOS) and the inclusion of the corresponding relativistic factors in the evolution equations. Such simulations further complements the recent efforts to describe crust-confined 3D magnetic field evolution without or with thermal evolution that used a simplified microphysical prescription described in the *PARODY*-based published works (Wood & Hollerbach 2015; Gourgouliatos, Wood & Hollerbach 2016; De Grandis et al. 2020; Gourgouliatos, Hollerbach & Igoshev 2020; De Grandis et al. 2021; Igoshev et al. 2021a, c). In particular, our simulations confirm the general trend seen from the initially purely small-scale field of Gourgouliatos et al. (2020), but using a more realistic model and performing a deeper analysis.

This paper is structured as follows. In Section 2, we briefly review the theoretical framework adopted to simulate the magneto-thermal evolution of NSs. The results of the first 3D coupled magneto-thermal evolution using *MATINS* are displayed in Section 3. Finally, we discuss our results and we draw the main conclusions in Section 4.

2 3D MAGNETO-THERMAL EVOLUTION

2.1 Basic equations

After few minutes from birth, NSs settle to a stratified, hydrodynamical static configuration, where no convection or differential rotation operate. If they are isolated, they have then no further relevant energy source, which implies that the kinetic (i.e. rotation), magnetic, and thermal energy will decay in the long term. In fact, all the rich multiwavelength phenomenology during the active life of NSs (beamed non-thermal emission, thermal X-ray emission, transient bursts, and flux enhancements) ultimately relies only on the electromagnetic torque and re-arrangement (via long-term dissipation and sporadic abrupt re-configurations) of the PNS huge magnetic energetic inheritance.

In order to quantify the long-term evolution of NS's magnetic fields $\vec{B}$ (in the crust) and the internal temperature T, the MHD equations can be then reduced to only two coupled equations (see the review by Pons & Viganò 2019 for more details), the Hall induction equation and the heat diffusion equation for the crust, which are, respectively,

$$\frac{\partial \vec{B}}{\partial t} = -\vec{\nabla} \times \left[\eta(T)\vec{\nabla} \times (e^{\nu}\vec{B}) + \frac{c}{4\pi e n_{\rm e}}[\vec{\nabla} \times (e^{\nu}\vec{B})] \times \vec{B}\right], \quad (1)$$

$$c_V(T)\frac{\partial (Te^{\nu})}{\partial t} = \vec{\nabla} \cdot (e^{\nu}\hat{\kappa}(T, \vec{B}) \cdot \vec{\nabla}(e^{\nu}T)) + e^{2\nu}(Q_J(\vec{B}, T) - Q_{\nu}(\vec{B}, T)), \quad (2)$$

where c is the speed of light, e the elementary electric charge, $n_{\rm e}$ the electron number density, $\eta(T) = c^2/(4\pi\sigma_e(T))$ the magnetic diffusivity (inversely proportional to the electrical conductivity σ_e), c_V the heat capacity per unit volume, $\hat{k}$ the anisotropic thermal conductivity tensor, Q_J and Q_{ν} the Joule heating rate and neutrino emissivity per unit volume, and e^{ν} is the relativistic redshift correction. While the Hall effect, along with the Ohmic dissipation and heat dissipation, governs the magneto-thermal evolution of NSs, a few other effects may become relevant under certain conditions. These include the thermoelectric effect (Biermann Battery) (Geppert & Wiebicke 1991, 1995; Wiebicke & Geppert 1991, 1992, 1996; Gourgouliatos, De Grandis & Igoshev 2022), crust yielding and deformation (Lander & Gourgouliatos 2019; Gourgouliatos & Lander 2021), and the interaction of the crust with the core and the magnetosphere [i.e. the expulsion of the core field due to superconductivity or ambipolar diffusion (Passamonti et al. 2016), and crust heating because of particle bombardment from magnetospheric currents (Beloborodov & Li 2016)].

The system of equations must be supplemented by an EOS, which allows to set: (i) the fixed, spherical background structure of the star (e.g. density and composition as a function of radius) which is obtained through solving the Tolman–Oppenheimer–Volkoff equation for a given central pressure (i.e. a given total mass), (ii) the local microphysics $\eta, c_V, \hat{\kappa}, Q_{\nu}$. Superfluid and superconductive models for neutrons and protons, respectively, must also be taken into account, since they have a huge impact on the cooling time-scales, via c_V and Q_{ν} In this study, we assume the superfluid models of Ho et al. (2015). EOS and superfluid models have an important impact on the cooling, but they play a lesser role in the magnetic field evolution (compared for instance to the chosen initial topology).

The main couplings between T and $\vec{B}$ in their evolution equations are explicitly marked as dependencies in the equations above. On one hand, a main effect is the magnetic-to-thermal energy conversion via Joule heating Q_J. This in turn depends on $\eta(T)$, which decreases as the NS cools down (and becomes basically temperature-independent for sufficiently low temperatures when impurities dominate the scattering processes, e.g. Aguilera, Pons & Miralles 2008). On the other hand, the magnetic field makes the thermal conductivity $\hat{\kappa}$ anisotropic, hampering the transmission of heat across the magnetic field lines and allowing important inhomogeneities in the surface temperature distribution T_s, for which observations can give constraints. At a much less extent, $\vec{B}$ has also an effect on c_V and Q_{ν}.

The core and the crust (accounting together for more than 99 per cent of mass and volume) are fully considered in the thermal evolution. For the outermost envelope, where the time-scales are much shorter than in the interior, we rely on the modelling of an effective function $T_s(T_b, \vec{B})$, which depends on the temperature and the magnetic field at the bottom of the envelope T_b (Potekhin, Pons & Page 2015a). We assume for simplicity a blackbody emission from

the surface, which might be a simplification (Potekhin, De Luca & Pons 2015b), but does not affect our conclusions.

We neglect the poorly known magnetic evolution in the core (see e.g. Gusakov, Kantor & Ofengeim 2020 and Wood & Graber 2022 for recent discussions), assuming that currents circulate only in the crust. Indeed, equation (1) is valid for the solid crust only: the first term is the Ohmic term, and the second is the non-linear Hall term, which is the effect of the Lorentz force acting on the ultra-relativistic electrons which carry the charge by freely moving through the solid (or plastic) ion lattice. The Hall term tends to push the electric currents towards the crust-core boundary, where the high impurity content and pasta phases could cause a fast dissipation of the magnetic field and therefore much less spin-down (Pons, Viganò & Rea 2013). In addition, the Hall term tends to redistribute the magnetic energy across all scales. This effect compensates the Ohmic dissipation of the smallest scales and, after $\mathcal{O}(10^4)$ yr, the crustal magnetic topology approaches a very slowly varying configuration, with the energy distributed over a broad range of multipoles, a Hall cascade with slope $\sim l^{-2}$ for the intermediate and small scales (Dehman et al. 2023a).

2.2 Numerical set-up

We use *MATINS* (Dehman et al. 2023a), a finite-volume 3D code employing the cubed-sphere coordinates, originally introduced by Ronchi, Iacono & Paolucci (1996). *MATINS* is designed for this scenario and evolves both the Hall induction and the heat diffusion equations (1) and (2) (see Dehman et al. 2023a and Ascenzi et al. in preparation for details about the magnetic and thermal evolution details separately). We consider the magnetic field confined in the crust employ potential magnetic boundary conditions (current-free magnetosphere) at the outer numerical boundary, placed at density $\rho = 10^{10}$ g cm^{-3} (close to the transition between liquid envelope and solid crust takes place for young or middle-age NSs). We implement the state-of-the-art calculations for the temperature-dependent electrical conductivity at each point of the star using Potekhin's public codes[1] (Potekhin et al. 2015a). The background NS model can be built using different models of the EOS at zero temperature, taken from the online public data base CompOSE[2] (CompStar Online Supernovae Equations of State). In particular, we will show results that employ a Skyrme-type model of EOS, SLy4 (Douchin & Haensel 2001), and we consider a mass $M = 1.4 M_{sun}$. We employ the $T_s(T_b, \vec{B})$ relation of Potekhin et al. (2015a) for iron magnetized envelopes. For more details on the impact of magnetized envelopes on the cooling of NSs, we refer the reader to Dehman et al. (2023b). The microphysics, star's structure, and envelope modules are the same as in our 2D models (Viganò et al. 2021).

We adopt a grid resolution of $N_r = 40$ and $N_\xi = N_\eta = 43$ per patch (a cubed-sphere has six patches), corresponding to a total number of resolved multipoles in the system of about $l_{max} \sim 40$. We follow the evolution for 100 kyr, an age where most NSs have cooled down enough to be hardly detectable (bolometric thermal luminosity $L < 10^{32}$ erg s^{-1}).

2.3 Initial topology

We start from the work by Reboul-Salze et al. (2021), who performed global simulations using MagIC (Wicht 2002). They consider a shell representative of the convective region of a PNS, and simulate the dynamo coming from the typical differential rotation profile seen during an advanced state of the core collapse. At saturation, they found a very complex topology, with most of the magnetic energy contained in the toroidal axisymmetric large-scale component (especially the quadrupolar component given by winding) and in the non-axisymmetric small- or medium-scale size magnetic structures, both for the toroidal and the poloidal components. The large-scale dipolar component represents only about ~ 5 per cent of the average magnetic field strength.

We adopt an initial field with an angular spectral energy distribution comparable to Reboul-Salze et al. (2021, fig. 7 top panel). Here, we indicate toroidal (blue)/poloidal (red) and axisymmetric (spherical harmonics order $m = 0$)/non-axisymmetric ($m \neq 0$) components as a function of the spherical harmonics degree l. In *MATINS*, although the evolved quantities are the magnetic field components, we prescribe the initial field in terms of the toroidal and poloidal decomposition, based on the Chandrasekhar–Kendall expressions:

$$\begin{aligned} \boldsymbol{B}_{\rm pol} &= \boldsymbol{\nabla} \times \left(\boldsymbol{\nabla} \times \Phi \boldsymbol{r}\right), \\ \boldsymbol{B}_{\rm tor} &= \boldsymbol{\nabla}\boldsymbol{\Psi} \times \boldsymbol{r}, \end{aligned} \tag{3}$$

where Φ and Ψ are the poloidal and toroidal scalar functions. Expanding Φ and Ψ as a series of spherical harmonics we have

$$\begin{aligned} \Phi(t, r, \theta, \phi) &= \frac{1}{r} \sum_{l,m} \Phi_{lm}(r, t) Y_{lm}(\theta, \phi) \\ \Psi(t, r, \theta, \phi) &= \frac{1}{r} \sum_{l,m} \Psi_{lm}(r, t) Y_{lm}(\theta, \phi), \end{aligned} \tag{4}$$

where $l = 1,..., l_{max}$ is the degree and $m = -l,..., l$ the order of the multipole. The initial configuration is then a smooth cascade in l (truncated for simplicity at $l = 20$) and m, with an exception for the quadrupolar toroidal component which dominates. The average initial magnetic field of a few 10^{14} G corresponds to a total magnetic energy of the order of $\sim 6 \times 10^{44}$ erg. Note that axial symmetry here refers to the rotational axis in the PNS phase, but the rigid rotation of the NS plays no role in the magnetic evolution (we do not evolve the full MHD, with the momentum equation, that includes the Coriolis force, since the background is assumed static for the solid crust). Therefore, hereafter, in our simulations, the reference axis can be thought of as the PNS rotational axis.

In the absence of a realistic core evolution, we simplify the topology by confining the magnetic field to the NS crust (smaller than the PNS shell). If the core evolution time-scales are much longer than the crust (see e.g. Gusakov et al. 2020), most results of the crustal evolution should hold anyway.

Since no specific information on the radial distribution of the magnetic energy is available in Reboul-Salze et al. (2021), we set an arbitrary set of initial poloidal $\Phi_{lm}(r)$ and toroidal $\Psi_{lm}(r)$ radial scalar functions (see appendix B of Dehman et al. 2023a for more details). For simplicity, as a standard choice we impose the radial profile of the dipolar poloidal scalar function, $\Phi_{l=1,m}(r)$, as in equation (8) of Aguilera et al. (2008):

$$\Phi_{l=1,m}(r) = \Phi_0 \, \mu \, r(a + tan(\mu R_\star) b), \tag{5}$$

where Φ_0 is the normalization and

$$a = \frac{sin(\mu r)}{(\mu r)^2} - \frac{cos(\mu r)}{\mu r}, \qquad b = -\frac{cos(\mu r)}{(\mu r)^2} - \frac{sin(\mu r)}{(\mu r)}, \tag{6}$$

μ is a parameter related to the magnetic field curvature that needs to be found for a given surface radius $R_\star$. For higher order multipoles

[1] http://www.ioffe.ru/astro/conduct/
[2] https://compose.obspm.fr/

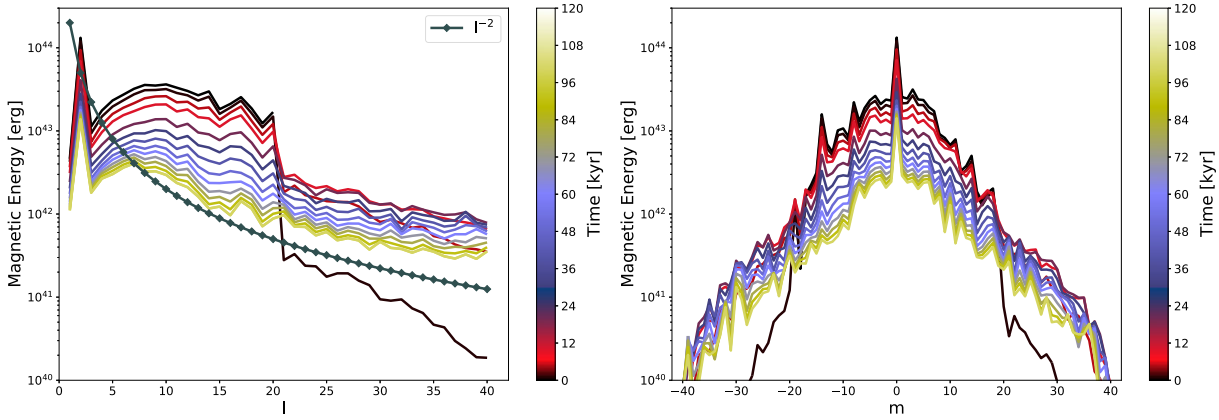

Figure 1. Spectrum of the total magnetic energy at different evolution time up to 100 kyr (Hall balance is reached in the system). Left panel: l – energy spectrum; right panel: m – energy spectrum.

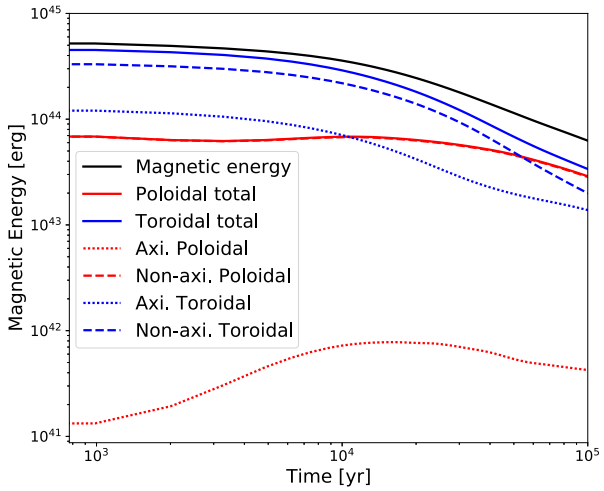

Figure 2. Decomposition of the poloidal and toroidal magnetic energy as a function of time. Poloidal magnetic energy is represented with red colour, the toroidal energy with blue, and the total magnetic energy with black solid lines. The dots correspond to the axisymmetric components of these energies and the dashed lines to the non-axisymmetric components. The axisymmetric and non-axisymmetric component are taken in PNS dynamo simulations with respect to the axis of the PNS rotation. This has no role in our simulations and we define these components with respect to the magnetic axis, starting with only $m = 0$ for a dipole.

of the poloidal scalar function ($l > 1$), and for all the toroidal scalar function contributions $\Psi_{lm}(r)$, we confine them inside the crust of an NS as follows:

$$\Phi_{l>1,m}(r),\, \Psi_{lm}(r) \propto -\big(R - r\big)^2 \big(r - R_c\big)^2, \tag{7}$$

where the proportionality means that every multipole can have a different normalization (i.e. its initial weight). Note that this particular choice has no specific physical ground, further than matching at $t = 0$ with a pure dipolar field at the surface. In order to test the sensitivity of the results on the initial radial function, we have also tested one case where the radial function for the dipolar poloidal component has been applied to all the other poloidal multipoles (producing an initial current sheet at the surface, see below).

Of course, it is unrealistic to expect that the birth NS configuration is given exactly by the ones simulated for the PNS stage. As a matter of fact, there is plenty of MHD time-scales to change the topology. On one hand, PNS will experience shrinking to the final NS size, which will probably imply an increase of the energy by flux conservation (here considered since we obtain similar volume-integrated energy spectra). On the other hand, the smaller scale will experience a fast decay as soon as the dynamo processes will stop feeding them. This is the reason why, to be conservative, we only consider the first $l \leq 20$ multipoles. However, the details of the spectral slope for the small scales are not important, since the Hall effect quickly regenerates them via direct cascade (Dehman et al. 2023a).

3 RESULTS

In this section, we present the results of our simulation assuming a crustal-confined initial field topology as described in Section 2.3. The studied model has an average magnetic field of a few 10^{14} G and a dominant Hall evolution (the magnetic Reynolds number is greater than unity and reaches a maximum of $R_m \sim 1600$ during evolution). For a more quantitative analysis of the 3D magnetic evolution, we survey the magnetic energy spectrum to observe the redistribution of the magnetic energy over the different spatial scales.

We examine at different evolution times the l and m energy spectrum, illustrated, respectively, in the left and right panels of Fig. 1. The transfer of the magnetic energy occur from large to small scales (the latter are initially empty): the direct cascade dominates. The magnetic energy spectra have reached a quasi-stationary state, i.e. the Hall-saturation, at about 20–30 kyr. Small-scale structures dissipate faster than large-scale ones, enhancing the Ohmic heating in the system. At the same time, the former are continuously fed by the latter, due to the Hall term in the induction equation. This is known as the Hall cascade; it happens due to the Hall-dominated dynamics and consists of an equilibrium distribution of magnetic energy, over a quite broad range of multipoles, with an approximate l^{-2} slope (Goldreich & Reisenegger 1992).

Throughout ∼100 kyr of evolution, the total magnetic energy drops by about half an order of magnitude as indicated in Fig. 2 (solid black line). We also display in the same figure the decomposition of the total magnetic energy (black) into its poloidal (red) and toroidal (blue) components. The dots correspond to the axisymmetric components ($m = 0$) and the dashed lines to the non-axisymmetric ones ($m \neq 0$). The studied initial topology has a poloidal field governed by its non-axisymmetric component, whereas the toroidal field has a significant contribution from both axisymmetric and non-axisymmetric pieces.

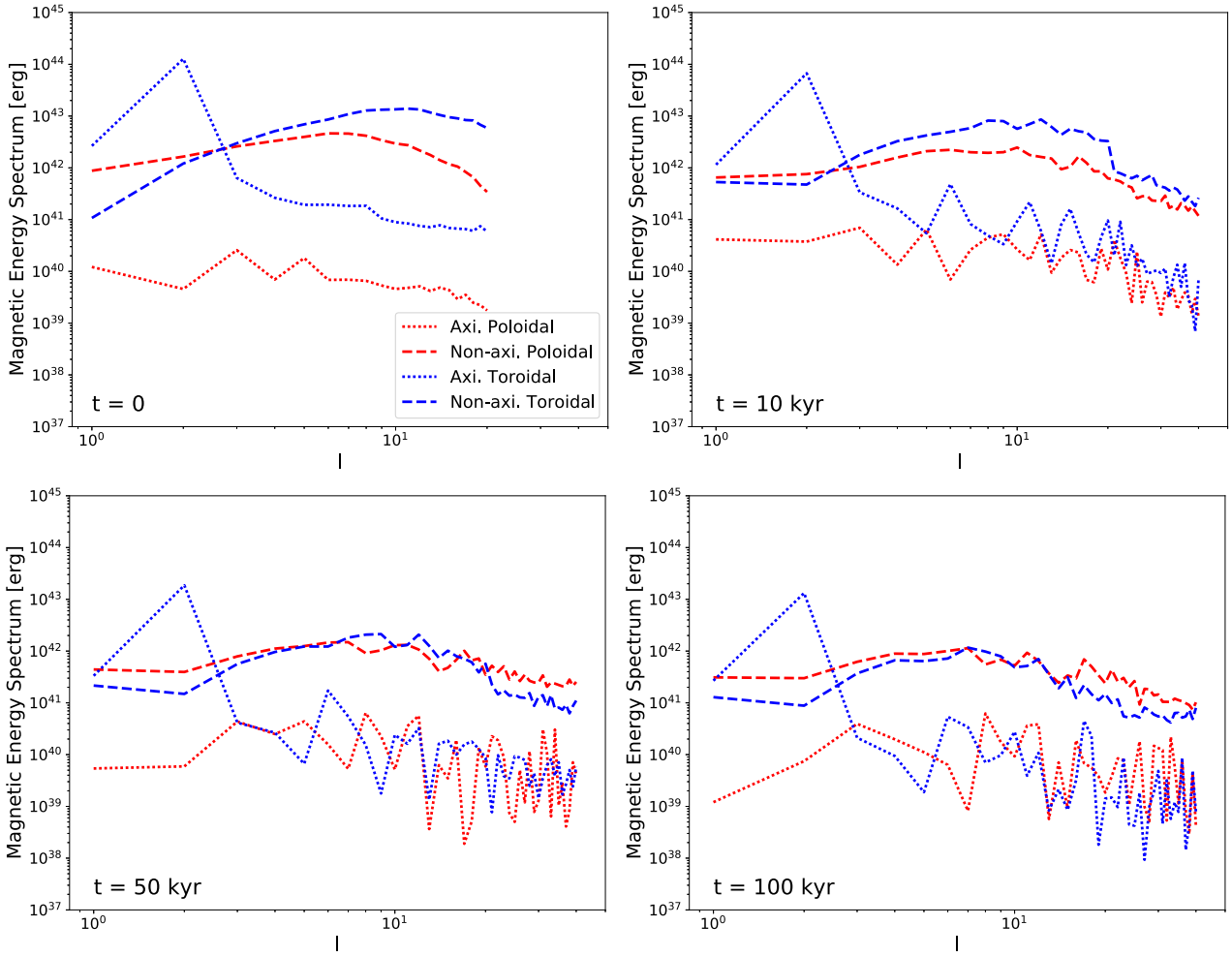

Figure 3. Spectrum of the toroidal magnetic energy (blue) and the poloidal magnetic energy (red) as a function of the spherical harmonics order l at $t = 0$, 10, 50, and 100 kyr. The dots correspond to the axisymmetric components of these energies and the dashed lines to the non-axisymmetric components. The total number of multipoles in the system is $l_{max} = 40$ and the initial number of multipoles is $l = 20$. The top left panel of this figure ($t = 0$) is inspired from a core-collapse generated turbulent field (Reboul-Salze et al. 2021, fig. 7 top panel).

For the first $\sim 10^4$ kyr, the dissipation of magnetic energy is relatively small compared to later time. One could notice that the magnetic energy is transferred from the toroidal to the poloidal field during the evolution. The most efficient transfer in terms of relative energy increase is for the poloidal axisymmetric field, probably because it is initially much weaker than the others. It shows a significant growth of one order of magnitude during the first 40–50 kyr. A saturation occurs for rest of the evolution (i.e. the system has reached the Hall balance). This quasi-constant energy trend appears for both the poloidal and the toroidal axisymmetric energy for $t \leq 50$ kyr. At the same time, a strong transfer of magnetic energy to the poloidal non-axisymmetric component takes place. The non-axisymmetric toroidal energy tends to dissipate faster than the total magnetic energy in the system. That is because part of the toroidal non-axisymmetric is transferred to the poloidal non-axisymmetric energy. The latter dominates the axisymmetric toroidal component at $\sim$10 kyr and the non-axisymmetric one at $\sim$50 kyr. Nevertheless, the total toroidal field governs the magnetic energy at all time (solid blue line).

For a further understanding, we study in Fig. 3 the evolution in time of the spectra. We display four snapshots of the toroidal (blue)/poloidal (red) and axisymmetric (dots)/non-axisymmetric (dashed lines) components as a function of the spherical harmonics degree l at different evolution time, e.g. $t = 0$, 10, 50, and 100 kyr. The angular spectral energy distribution at t=0 is comparable to Reboul-Salze et al. (2021, fig. 7 top panel). At $\sim$10 kyr, a transfer of energy to the non-axisymmetric toroidal dipole (blue dashed line, $l = 1$) takes place due to the inverse Hall cascade. A significant transfer of energy to the poloidal axisymmetric field happens at large and small scales. Instead, at late time (Hall balance is reached in the system) the dipolar component dissipates. For a better understanding, we discuss the behaviour of small and large scales independently. During the evolution, the small-scale modes ($10 \leq l \leq 40$) gain a significant fraction of the magnetic energy due to the Hall cascade in the system. The different behaviours are listed next.

(i) At $t = 10$ kyr, both toroidal components (i.e. axisymmetric and non-axisymmetric) decay in time, whereas the two poloidal components gain energy at small scales. That also agrees with Fig. 2 and indicates equipartition at small scales, since isotropy is easier to achieve. As a matter of fact, the peculiar crust geometry (a thin

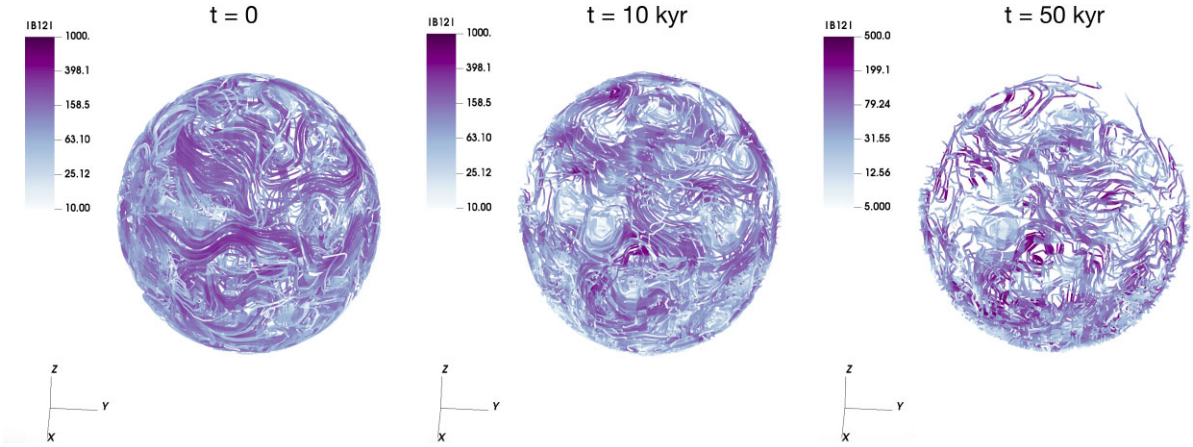

Figure 4. Field lines in the crust of an NS at $t = 0$ (on the left), $t = 10$ kyr (in the centre), and $t = 50$ kyr (on the right). The colour scales indicates the local field intensity in units of 10^{12} G.

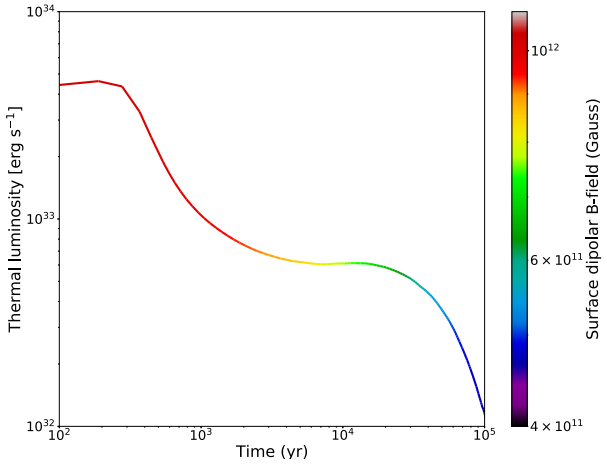

Figure 5. Luminosity curve as a function of time. The colourbar indicates the evolution of the dipolar component of the poloidal magnetic field at the surface of the star (value at the magnetic pole).

shell of ∼1 km) and the strong stratification play against isotropy and therefore equipartition between large-scale components.

(ii) At about 40–50 kyr, the system approaches a Hall-balance (see also Fig. 1). At this stage, one can notice a slightly different behaviour for the axisymmetric and the non-axisymmetric components. On one hand, the axisymmetric components reach an approximate equipartition of the magnetic energy between poloidal and toroidal components at small scales. That is in agreement to what was found using the axisymmetric 2D code (Pons & Viganò 2019). A change of phase in the oscillations occur on a time-scale of 40–50 kyr. On the other hand, for the non-axisymmetric modes, the slight toroidal dominance over poloidal seen at 10 kyr inverts at 50 and 100 kyr. That is due to a transfer of energy from toroidal to poloidal field which, however, can be interpreted as equipartition of energy on the small isotropic scales.

Minor differences appear in the spectrum at 50 and 100 kyr and that is because the system has reached the Hall balance and the spectra remains stationary as it is shown in Fig. 1. Note also how the large scales barely evolve, compared to the others. This is another confirmation that the NS tends to a universal behaviour (Hall cascade) for intermediate and small scales, but it has a strong memory of the large-scale magnetic topology at birth (Dehman et al. 2023a). This has important implications to relate current observables to the formation process (PNS stage).

The field lines in the crust of an NS at $t = 0$, 10, and 50 kyr are displayed in Fig. 4. The magnetic field lines are highly multipolar and many small-scale structures cover the surface. The field lines are very tangled throughout evolution, making it difficult to discern any clear dominant component.

In Fig. 5, we show the evolution of the thermal luminosity and (in colour scale) of B_{pol}^{dip}, the dipolar component of the poloidal magnetic field at the surface of the star (value at the magnetic pole). For such an initial configuration, the luminosity ranges from 5×10^{32} to 10^{33} erg s^{-1} in the neutrino cooling era, soon after, in the photon cooling era ($t \sim 10^5$) yr, the luminosity drops sharply below 10^{32} erg s^{-1}. The rapid cooling during the photon cooling era is also caused by the low core heat capacity, which in turn depends on the assumed pairing details. A comprehensive revision of the microphysics embedded in magneto-thermal models can be found in Potekhin et al. (2015a). On the other hand, B_{pol}^{dip} drops from $\sim 10^{12}$ to $\sim 4 \times 10^{11}$ G without any noticeable increase.

At the surface of the star, we define the average field strength in each multipole l as follows:

$$\bar{B}_l^{surf} = \left[\frac{1}{4\pi}\int \mathrm{d}\Omega (B_r^2 + B_\theta^2 + B_\phi^2)\right]^{0.5} = \left[\frac{B_0^2}{4\pi}\sum_m (b_l^m)^2 \left(e^{-2\lambda(R)}(l+1)^2 + l(l+1)\right)\right]^{0.5}, \quad (8)$$

where $e^{-2\lambda(R)}$ is the relativistic metric correction at the surface, b_l^m are the dimensionless weights of the multipoles entering in the spherical harmonics decomposition of the radial magnetic field, and B_0 is the normalization used in the code (see equation 26 of Dehman et al. 2023a for more details). In the top panel of Fig. 6, we show the time evolution of $\bar{B}_l^{surf}$ as a function of l. At t = 0, the NS surface is dominated by the dipolar mode due to the specific radial function that we assume for each multipole in this case. However, as soon as we start the evolution the small-scale modes become dominant at about 1 kyr. Then the system reaches some sort of balance throughout the evolution. The balanced configuration is dominated by small-scale structures only ($l \geq 10$). This finding implies that during the evolution the B_{pol}^{dip} value (the colourbar of Fig. 5) is much weaker

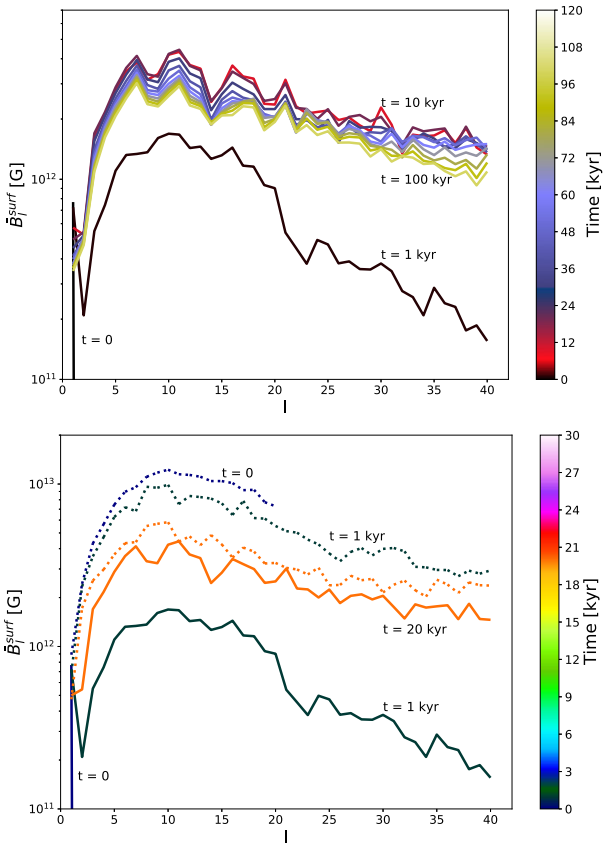

Figure 6. Time evolution of the surface average field strength as a function of l (equation 8). Top panel: evolution up to 100 kyr. The colourbar reflects the evolution in time. Bottom panel: comparison of the evolution for different radial functions at $t = 0$ (black), 1 kyr (red), and 20 kyr (yellow). The solid lines correspond to the radial function that fits the potential boundary conditions (Dehman et al. 2023a, appendix B) and results in an initial purely dipolar field at surface (black solid lines), whereas the dots correspond to Aguilera et al. (2008, equation 8) applied to both toroidal and poloidal field. The latter allows an initial distribution of small- and large-scale multipoles on the star's surface.

than the one inferred for most magnetars (10^{14}–10^{15} G), when the classical spin-down formula is used to interpret the timing properties.

So far we have focused only on different choices of the tangential distribution of magnetic energy (the initial multipole weights). However, the initial radial profile of the topology (i.e. the set of radial functions of each multipole (l, m)) is also an important parameter that potentially affects our results (also connected to the outer and inner boundary conditions). For this reason, in the bottom panel of Fig. 6, we compare the evolution for two different initial sets of radial functions (both equally arbitrary), which result in very different initial shapes of $\bar{B}_l^{surf}$. The solid lines correspond to a set of radial functions that allow a smooth matching with a pure dipole outside (see appendix B of Dehman et al. 2023a), confining inside all the other multipoles. The dots correspond to another set of radial functions that allows an initial distribution of small- and large-scale multipoles on the star's surface, with an initial non-zero tangential current that is quickly dissipated by the re-arrangement of the field. Both simulations are soon (∼1 kyr, red) dominated by the small-scale structures and approach a similar spectral distribution of $\bar{B}_l^{surf}$ after about 20 kyr, when the Hall balance is reached. From the comparison of these two simple choices, it seems that, independently from the initial radial distribution of the magnetic field inside the NS's crust, the star surface is anyway dominated by small-scale structures.

4 DISCUSSION

In the previous work (Dehman et al. 2023a), we have explored different initial field configurations using *MATINS*. Our simulations confirmed that the spectra and topology of the magnetic field keep a strong memory of the initial large scales, which are much harder to be restructured or created. This indicates that the type of large-scale configurations attained during the PNS stage and the NS formation is crucial to determine the magnetic field topology at any age of its long-term evolution. Dynamo simulations of PNS show a complex field configuration in which most of the energy is stored in the toroidal field and only a small fraction (∼ 5 per cent) of it is stored in the dipole component, with small-scale components dominating over the large-scale ones (in particular, the dipolar poloidal component responsible for the spin-down).

To assess how such complex initial topology evolves, we presented the first coupled 3D magneto-thermal simulation of an NS field evolution, starting from a configuration similar (in energy spectra) to the recent PNS dynamo simulations by Reboul-Salze et al. (2021). We include the most realistic background structure and microphysical ingredients so far. We perform a long-term simulation until the age of ∼100 kyr, i.e. until the Hall balance is reached and the luminosity evolution is driven by mostly by photon cooling.

Following the analysis of our results (Section 3), we found that the surface dipolar component experiences no relevant growth in time in this time-scale, independently from the initial radial distribution of the magnetic field in the NS crust (see Fig. 6, bottom panel). We argue that only starting from an initial magnetic energy distribution mostly concentrated in the dipolar component alone (in the crust or in the core) *could* result in a dominant surface dipolar magnetic field. As in our previous work, and in PARODY-based studies (Gourgouliatos et al. 2020; Igoshev et al. 2021c), we find a wide range of spatial scales over which the magnetic energy is distributed, and the large-scale components are sub-dominant. However, it is unclear how core collapse could yield to an NS with such an almost pure dipolar configuration. Indeed, several observations suggest that internal non-dipolar components (toroidal and multipolar components) are dominant: low field magnetars (Rea et al. 2013; Tan et al. 2023), high-B pulsars (Zhu et al. 2011), CCO with outbursts (Rea et al. 2016), spectral features in magnetars (Tiengo et al. 2013), and X-ray Dim Isolated NSs (XDINS) (Borghese et al. 2017). At last, in Dehman et al. (2020), the 2D simulations showed that B_{pol}^{dip} played a minor role in determining magnetars bursting activity and the magnetic energy stored in the crust of the star is a better indicator.

These features, already partially explored in Gourgouliatos et al. (2020) and Igoshev et al. (2021c) (where they started with only small-scale multipoles), could be suitable for describing CCOs, X-ray sources with luminosity ranging between 10^{32} and 10^{34} erg s^{-1}, located at the centres of supernova remnants, with an estimated surface dipole magnetic field in the range 10^{10}–10^{11} G. The dissipation of such weak large-scale component alone cannot provide sufficient thermal energy to power their observed X-ray luminosity. It is believed instead that CCOs have a hidden strong magnetic field due to the fall-back accretion (Ho 2011; Viganò & Pons 2012). This magnetic field dissipates in the star interior to provide the bright thermal luminosity of CCOs (Fig. 5).

We may consider that some other physical effects could act during the collapse or in the early NS life, to provide at the surface of the star large-scale dipole $B_{pol}^{dip} \gg 10^{13}$ G. Strong inverse cascade

could be triggered by helical magnetic fields (e.g. Brandenburg 2020 for box simulations with no stratification), but it has not been seen so far in global simulations. We might be missing some important dynamics able to have a large-scale organization of the sustaining currents. On one hand, the PNS dynamo simulations are intrinsically affected by the chosen simple boundary conditions (see e.g. Raynaud et al. 2020 for a comparison between perfect conductor and potential configuration), which are anyway not realistic for the dirty, dense, and hot plasma-filled environment of the PNS. On the other hand, the field sustained by currents in the core might be relevant, especially in the long-term, since its evolution time-scales are arguably longer (but see Gusakov et al. 2020). However, it is unclear how to generate a strong poloidal dipolar field (supported by strong toroidal and organized currents) during the PNS or early NS stages.

A radically different alternative is possible, compatible with the absence of strong dipolar fields. The values of B_{pol}^{dip} might indeed always be lower if the electromagnetic torque is dominated by magnetospheric effects, like particle winds and the presence of strong and extended loops, charges of particles. Indeed, for the Sun (Yeates et al. 2018) and for Zeeman–Doppler studies of main-sequence stars (Donati et al. 2009) inferred magnetospheric topology show field lines stretched by the wind and complex topologies. Strong magnetospheric structures could also be compatible with the presence of tiny hotspots (radii less than 1 km), commonly inferred from magnetars' X-ray thermal spectra (in quiescence or outburst), and with the more studied resonant Compton scattering causing the observed non-thermal tails in spectra. However, quantifying the additional magnetospheric contributions to the spin-down is so far limited by the models of Tong et al. (2013), and more work is needed in this sense to support this scenario. Along this line, the coupling of the interior evolution with the magnetosphere is essential to allow the currents to flow and the surface dipolar field to be larger (Akgün et al. 2018; Urbán et al. 2023).

ACKNOWLEDGEMENTS

CD has the partial support of NORDITA while working on this article. CD, SA, and NR are supported by the ERC Consolidator Grant 'MAGNESIA' No. 817661 (PI: N. Rea) and this work has been carried out within the framework of the doctoral program in Physics of the Universitat Autònoma de Barcelona and it is partially supported by the program Unidad de Excelencia María de Maeztu CEX2020-001058-M. DV is supported by the European Research Council (ERC) under the European Union's Horizon 2020 research and innovation programme (ERC Starting Grant IMAGINE' No. 948582, PI: DV). JAP acknowledges support from the Generalitat Valenciana grants ASFAE/2022/026 (with funding from NextGenerationEU PRTR-C17.I1) and the AEI grant PID2021-127495NB-I00.

DATA AVAILABILITY

All data produced in this work will be shared on reasonable request to the corresponding author.

REFERENCES

Aguilera D. N., Pons J. A., Miralles J. A., 2008, ApJ, 673, L167
Akgün T., Cerdá-Durán P., Miralles J. A., Pons J. A., 2018, MNRAS, 481, 5331
Akiyama S., Wheeler J. C., Meier D. L., Lichtenstadt I., 2003, ApJ, 584, 954
Aloy M. Á., Obergaulinger M., 2021, MNRAS, 500, 4365
Balbus S. A., Hawley J. F., 1991, ApJ, 376, 214
Barrère P., Guilet J., Reboul-Salze A., Raynaud R., Janka H. T., 2022, A&A, 668, A79
Becerra L., Reisenegger A., Valdivia J. A., Gusakov M. E., 2022, MNRAS, 511, 732
Beloborodov A. M., Li X., 2016, ApJ., 833, 261
Borghese A., Rea N., Coti Zelati F., Tiengo A., Turolla R., Zane S., 2017, MNRAS, 468, 2975
Brandenburg A., 2020, ApJ, 901, 18
Bugli M., Guilet J., Obergaulinger M., Cerdá-Durán P., Aloy M. A., 2020, MNRAS, 492, 58
Burrows A., Lattimer J. M., 1986, ApJ, 307, 178
De Grandis D., Turolla R., Wood T. S., Zane S., Taverna R., Gourgouliatos K. N., 2020, ApJ, 903, 40
De Grandis D., Taverna R., Turolla R., Gnarini A., Popov S. B., Zane S., Wood T. S., 2021, ApJ, 914, 118
Dehman C., Viganò D., Rea N., Pons J. A., Perna R., Garcia-Garcia A., 2020, ApJ, 902, L32
Dehman C., Viganò D., Pons J. A., Rea N., 2023a, MNRAS, 518, 1222
Dehman C., Pons J. A., Viganò D., Rea N., 2023b, MNRAS, 520, L42
Douchin F., Haensel P., 2001, A&A, 380, 151
Ferrario L., Wickramasinghe D., 2006, MNRAS, 367, 1323
Geppert U., Wiebicke H. J., 1991, A&AS, 87, 217
Geppert U., Wiebicke H. J., 1995, A&A, 300, 429
Goldreich P., Reisenegger A., 1992, ApJ, 395, 250
Gourgouliatos K. N., Lander S. K., 2021, MNRAS, 506, 3578
Gourgouliatos K. N., Wood T. S., Hollerbach R., 2016, Proc. Natl. Acad. Sci., 113, 3944
Gourgouliatos K. N., Hollerbach R., Igoshev A. P., 2020, MNRAS, 495, 1692
Gourgouliatos K. N., De Grandis D., Igoshev A., 2022, Symmetry, 14, 130
Gusakov M. E., Kantor E. M., Ofengeim D. D., 2020, MNRAS, 499, 4561
Ho W. C., 2011, MNRAS, 414, 2567
Ho W. C., Elshamouty K. G., Heinke C. O., Potekhin A. Y., 2015, Phys. Rev. C, 91, 015806
Igoshev A. P., Hollerbach R., Wood T., Gourgouliatos K. N., 2021a, Nat. Astron., 5, 145
Igoshev A. P., Popov S. B., Hollerbach R., 2021b, Universe, 7, 351
Igoshev A. P., Gourgouliatos K. N., Hollerbach R., Wood T. S., 2021c, ApJ, 909, 101
Janka H.-T., 2012, Annu. Rev. Nucl. Part. Sci., 62, 407
Keil W., Janka H. T., 1995, A&A, 296, 145
Lander S. K., Gourgouliatos K. N., 2019, MNRAS, 486, 4130
Makarenko E. I., Igoshev A. P., Kholtygin A. F., 2021, MNRAS, 504, 5813
Masada Y., Takiwaki T., Kotake K., 2022, ApJ, 924, 75
Mösta P. et al., 2014, ApJ, 785, L29
Mösta P., Ott C. D., Radice D., Roberts L. F., Schnetter E., Haas R., 2015, Nature, 528, 376
Donati J.-F., Jardine M., Gregory S., Bouvier J., Dougados C., Ménard F., 2009, in Neiner C., Zahn J.-P., eds, EAS Publ. Ser. Vol. 39, Accretion Discs, Low-Mass Protostars and Planets: Probing the Impact of Magnetic Fields on Stellar Formation. Cambridge Univ. Press, Cambridge, p. 133
Obergaulinger M., Aloy M. Á., 2020, MNRAS, 492, 4613
Obergaulinger M., Aloy M. Á., 2022, MNRAS, 512, 2489
Obergaulinger M., Janka H. T., Aloy M. A., 2014, MNRAS, 445, 3169
Passamonti A., Akgün T., Pons J. A., Miralles J. A., 2016, MNRAS, 465, 3416
Pons J. A., Viganò D., 2019, Living Rev. Comput. Astrophys., 5, 3
Pons J. A., Reddy S., Prakash M., Lattimer J. M., Miralles J. A., 1999, ApJ, 513, 780
Pons J. A., Viganò D., Rea N., 2013, Nat. Phys., 9, 431
Potekhin A. Y., Pons J. A., Page D., 2015a, Space Sci. Rev., 191, 239
Potekhin A. Y., De Luca A., Pons J. A., 2015b, Space Sci. Rev., 191, 171
Powell J., Mueller B., Aguilera-Dena D. R., Langer N., 2023, MNRAS, 522, 6070
Raynaud R., Guilet J., Janka H.-T., Gastine T., 2020, Sci. Adv., 6, eaay2732
Rea N. et al., 2013, ApJ, 770, 65
Rea N., Borghese A., Esposito P., Zelati F. C., Bachetti M., Israel G. L., De Luca A., 2016, ApJ, 828, L13

Reboul-Salze A., Guilet J., Raynaud R., Bugli M., 2021, A&A, 645, A109
Rembiasz T., Obergaulinger M., Guilet J., Cerdá-Durán P., Aloy M. A., Müller E., 2017, Acta Phys. Pol. B, 10, 361
Ronchi C., Iacono R., Paolucci P., 1996, J. Comput. Phys., 124, 93
Schneider F., Ohlmann S. T., Podsiadlowski P., Röpke F. K., Balbus S. A., Pakmor R., Springel V., 2019, Nature, 574, 211
Shultz M. E. et al., 2018, MNRAS, 475, 5144
Tan C., Rigoselli M., Esposito P., Stappers B., 2023, MNRAS, 520, 5960
Tiengo A. et al., 2013, Nature, 500, 312
Tong H., Xu R., Song L., Qiao G., 2013, ApJ, 768, 144
Urbán J. F., Stefanou P., Dehman C., Pons J. A., 2023, MNRAS, in press
Viganò D., Pons J. A., 2012, MNRAS, 425, 2487
Viganò D., Garcia-Garcia A., Pons J. A., Dehman C., Graber V., 2021, Comput. Phys. Commun., 265, 108001
Wicht J., 2002, Phys. Earth Planet. Inter., 132, 281
Wiebicke H. J., Geppert U., 1991, A&A, 245, 331
Wiebicke H. J., Geppert U., 1992, A&A, 262, 125
Wiebicke H. J., Geppert U., 1996, A&A, 309, 203
Wood T. S., Graber V., 2022, Universe, 8, 228
Wood T. S., Hollerbach R., 2015, Phys. Rev. Lett., 114, 191101
Yeates A. R. et al., 2018, Space Sci. Rev., 214, 99
Zhu W., Kaspi V. M., McLaughlin M. A., Pavlov G. G., Ng C.-Y., Manchester R. N., Gaensler B. M., Woods P. M., 2011, ApJ, 734, 44

This paper has been typeset from a TEX/LATEX file prepared by the author.